

# Gravitational field calculation in spherical coordinates using variable densities in depth

Santiago R. Soler<sup>1,2</sup>, Agustina Pesce<sup>1,2</sup>, Leonardo Uieda<sup>3</sup> and Mario E. Gimenez<sup>1,2</sup>

<sup>1</sup>CONICET, Argentina. e-mail: [santiago.r.soler@gmail.com](mailto:santiago.r.soler@gmail.com)

<sup>2</sup>Instituto Geofísico Sismológico Volponi, Universidad Nacional de San Juan, Argentina

<sup>3</sup>Department of Earth Sciences, SOEST, University of Hawai'i at Mānoa, Honolulu, Hawaii, USA

16 October 2018

## SUMMARY

We present a new methodology to compute the gravitational fields generated by tesseroids (spherical prisms) whose density varies continuously with depth according to an arbitrary function. It approximates the gravitational fields through the Gauss-Legendre Quadrature along with two discretization algorithms that automatically control its accuracy by adaptively dividing the tesseroid into smaller ones. The first one is a preexisting adaptive discretization algorithm that reduces the errors due to the distance between the tesseroid and the computation point. The second is a new density-based discretization algorithm that decreases the errors introduced by the variation of the density function with depth. The amount of divisions made by each algorithm is indirectly controlled by two parameters: the distance-size ratio and the delta ratio. We have obtained analytical solutions for a spherical shell with radially variable density and compared them to the results of the numerical model for linear and exponential density functions. These comparisons allowed us to obtain optimum values for the distance-size and delta ratios that yield an accuracy of 0.1% of the analytical solutions. The resulting optimal values of distance-size ratio for the gravitational potential, its gradient, and Marussi tensor are 1, 2 and 8, respectively. A delta ratio of 0.2 is needed for the computation of the gravitational potential and its gradient components, while a value of 0.01 must be used for the Marussi tensor components. Lastly, we apply this new methodology to model the Neuquén Basin, a foreland basin in Argentina with a maximum depth of over 5000 m, using an exponential density function.

**Key words:** Numerical modelling, Numerical approximations and analysis, Gravity anomalies and Earth structure, Satellite gravity

## 1 INTRODUCTION

The lithosphere's density variation with depth has been studied for close to a century. Over this time period, several density-depth relations have been proposed for different rock types (e.g., [Maxant 1980](#); [Rao 1986](#); [Rao et al. 1993, 1994](#)). Furthermore, depth-variable densities have been used in forward and inverse gravity modelling, mostly applied to sedimentary basins ([Cordell 1973](#); [Rao 1986](#); [Cowie & Karner 1990](#); [Rao et al. 1993, 1994](#); [Zhang et al. 2001](#); [Welford et al. 2010](#)). These forward gravity models have been developed for two or three dimensional bodies in Cartesian coordinates, which limits the applications to local scales. The advent of satellite gravimetry has provided gravity field measurements with global coverage, enabling modelling and interpretation on regional and global scales. Hence, designing forward modelling methods that reproduce the gravity anomalies for such scales is of high importance.

To take into account the curvature of the Earth, many global forward modelling methods are defined in geocentric spherical coordinates. A common approach is to discretize the Earth into

tesseroids (spherical prisms), which are defined by pairs of latitude, longitude, and radial boundaries (see Fig. 1). The gravitational fields generated by an arbitrary tesseroid on any external point are given by volume integrals that must be numerically approximated. The literature offers two main approaches: one involves Taylor series expansion ([Heck & Seitz 2007](#); [Grombein et al. 2013](#)) while the other makes use of Gauss-Legendre Quadrature (GLQ) ([Asgharzadeh et al. 2007](#); [Wild-Pfeiffer 2008](#); [Li et al. 2011](#); [Uieda et al. 2016](#)). The Taylor series expansion is not well suited to develop an algorithm for a density varying with depth according to an arbitrary function. Different series expansion terms would have to be obtained for each density function desired. Conversely, an arbitrary density function can be included in the GLQ without any change to the integration method.

The main challenge of the GLQ integration is loss of accuracy when the computation point gets closer to the tesseroid ([Ku 1977](#)). [Uieda et al. \(2016\)](#) built on the adaptive discretization algorithm of [Li et al. \(2011\)](#) to automatically obtain integration results with 0.1% accuracy. The algorithm consist in recursively splitting the tesseroid into smaller ones when a threshold is exceeded, namely

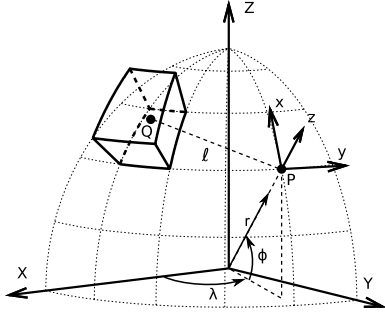


**Figure 1.** A tesseroide (spherical prism) in a geocentric spherical coordinate system, with a computation point  $P$  and its local north oriented Cartesian coordinate system. After Uieda (2015).

when the normalized distance to the computation point is greater than a “distance-size ratio” ( $D$ ). Uieda et al. (2016) have also obtained standard values of  $D$  for the gravitational potential, acceleration, and gradient tensor components by comparing the numerical model with the fields generated by a spherical shell.

We present a new algorithm for computing the gravitational fields generated by any tesseroide with an arbitrary continuous density function on any external point. It is based on the GLQ approximation and the adaptive discretization of Uieda et al. (2016), which we extend to include a new density-based discretization step. In order to ensure the accuracy of the numerical approximation we have determined optimal values for the controlling parameters by comparing the numerical approximation with analytical solutions for spherical shells. Finally, we applied the methodology to model the Neuquén basin, Argentina, using tesseroides with an exponentially increasing density with depth.

## 2 METHODOLOGY

We define an external computation point  $P(r, \phi, \lambda)$  in a geocentric spherical coordinate system at a radius  $r$ , geocentric latitude  $\phi$ , and longitude  $\lambda$  where the gravitational fields are going to be calculated. The first and second derivatives of the gravitational potential are taken with respect to the local north-oriented Cartesian coordinate system of  $P$  (Fig. 1). Grombein et al. (2013) provide efficient formulations for the volume integrals of the gravitational potential and its first and second derivatives of a tesseroide with homogeneous density. Here, we will assume that the tesseroide has a density varying with  $r$  according to an arbitrary function  $\rho(r)$ . Thus, the integrals for the gravitational fields are slightly modified to

$$V(r, \phi, \lambda) = G \int_{\lambda_1}^{\lambda_2} \int_{\phi_1}^{\phi_2} \int_{r_1}^{r_2} \frac{\rho(r')}{\ell} \kappa dr' d\phi' d\lambda', \quad (1)$$

$$g_\alpha(r, \phi, \lambda) = G \int_{\lambda_1}^{\lambda_2} \int_{\phi_1}^{\phi_2} \int_{r_1}^{r_2} \rho(r') \frac{\Delta_\alpha}{\ell^3} \kappa dr' d\phi' d\lambda', \quad (2)$$

and

$$g_{\alpha\beta}(r, \phi, \lambda) = G \int_{\lambda_1}^{\lambda_2} \int_{\phi_1}^{\phi_2} \int_{r_1}^{r_2} \rho(r') I_{\alpha\beta} \kappa dr' d\phi' d\lambda', \quad (3)$$

in which

$$I_{\alpha\beta} = \left( \frac{3\Delta_\alpha \Delta_\beta}{\ell^5} - \frac{\delta_{\alpha\beta}}{\ell^3} \right), \quad (4)$$

$\alpha, \beta \in \{x, y, z\}$ ,  $\delta_{\alpha\beta}$  is Kronecker's delta,  $G = 6.674 \times 10^{-11} \text{ m}^3 \text{ kg}^{-1} \text{ s}^{-1}$  is the gravitational constant and

$$\Delta_x = r' [\cos \phi \sin \phi' - \sin \phi \cos \phi' \cos(\lambda' - \lambda)], \quad (5)$$

$$\Delta_y = r' \cos \phi' \sin(\lambda' - \lambda), \quad (6)$$

$$\Delta_z = r' \cos \psi - r, \quad (7)$$

$$\kappa = r'^2 \cos \phi', \quad (8)$$

$$\ell = \sqrt{r'^2 + r^2 - 2rr' \cos \psi}, \quad (9)$$

$$\cos \psi = \sin \phi \sin \phi' + \cos \phi \cos \phi' \cos(\lambda' - \lambda). \quad (10)$$

### 2.1 Gauss-Legendre Quadrature integration

Applying a  $N$ th order GLQ, we can approximate each integral in equations 1, 2 and 3 by a weighted sum of the integration kernel evaluated on the roots of an  $N$ th order Legendre polynomial (Hildebrand 1987, p. 390). Unlike the homogeneous density case, the radial density function  $\rho(r)$  must also be included in the integration and evaluated on the Legendre polynomial roots (i.e., quadrature nodes).

$$\begin{aligned} \iiint_{\Omega} \rho(r') f(r', \phi', \lambda') d\Omega \approx \\ A \sum_{i=1}^{N^r} \sum_{j=1}^{N^\phi} \sum_{k=1}^{N^\lambda} W_i^r W_j^\phi W_k^\lambda \rho(r_i) f(r_i, \phi_j, \lambda_k), \end{aligned} \quad (11)$$

where

$$A = \frac{(\lambda_2 - \lambda_1)(\phi_2 - \phi_1)(r_2 - r_1)}{8}, \quad (12)$$

$(r_i, \phi_j, \lambda_k)$  are the quadrature nodes, and  $W_i^r$  are the quadrature weights.

### 2.2 Adaptive Discretization

Ku (1977) noticed that the GLQ integration becomes less accurate when the computation point is closer to the mass element. One way to prevent this from happening would be to increase the GLQ order. Doing so would uniformly increase the number of point masses inside the tesseroide volume. However, an increase in the point mass concentration is only required close to the computation point (Uieda et al. 2016). Alternatively, Li et al. (2011) proposed an adaptive discretization algorithm which keeps the GLQ order fixed

and divides the tesseroid based on a ratio between the distance to the computation point and its dimensions. This algorithm produces a more efficient computation because an increased concentration of point masses is produced where it is needed more. Uieda et al. (2016) developed a modified version of this algorithm, which we will use here. What follows is a summary of the algorithm and the reader is referred to Uieda et al. (2016) for a detailed description.

The following algorithm computes the gravitational fields at a given point at  $(r, \phi, \lambda)$  due to a tesseroid with its geometric centre at  $(r_t, \phi_t, \lambda_t)$  and dimensions  $L_r$ ,  $L_\phi$ , and  $L_\lambda$  given by

$$L_\lambda = r_2 \arccos(\sin^2 \phi_t + \cos^2 \phi_t \cos(\lambda_2 - \lambda_1)), \quad (13)$$

$$L_\phi = r_2 \arccos(\sin \phi_2 \sin \phi_1 + \cos \phi_2 \cos \phi_1), \quad (14)$$

and

$$L_r = r_2 - r_1. \quad (15)$$

*Step 1:* Check that the tesseroid satisfies the following inequality for each dimension  $L_i$  of the tesseroid:

$$\frac{d}{L_i} \geq D, \quad (16)$$

in which  $D$  is a positive scalar called the distance-size ratio and  $d$  is the distance between the computation point and the geometric centre of the tesseroid

$$d = [r^2 + r_t^2 - 2rr_t \cos \psi_t]^{\frac{1}{2}}, \quad (17)$$

$$\cos \psi_t = \sin \phi \sin \phi_t + \cos \phi \cos \phi_t \cos(\lambda - \lambda_t). \quad (18)$$

*Step 2:* If none of the dimensions of the tesseroid fail inequality 16, then compute the gravitational effect of the tesseroid using a second-order GLQ (Eq. 11). Add the computed effect to a running total.

*Step 3:* If any dimension fails inequality 16, split the tesseroid in half along the offending dimensions. Repeat steps 1-3 for all smaller tesseroids until none are left.

*Final step:* By the end of the algorithm, the running total will be the gravitational effect of the tesseroid.

Notice that the distance-size ratio  $D$  determines how many times the tesseroids will be divided. Therefore, it effectively regulates both the accuracy of the algorithm and its computation time. An optimal value for  $D$  cannot be directly calculated from the desired accuracy level. Instead, it is empirically determined by comparing the numerical results with the analytical solution for a spherical shell. Uieda et al. (2016) used a shell with homogeneous density to determine optimal values of  $D$ . Here, we will repeat the numerical experiment using analytical expressions for shells with density varying according to exponential and linear functions of  $r$ .

### 2.3 Density-based Discretization Algorithm

The numerical integration of an arbitrary density function introduces a new type of problem: the integration error from using only a few nodes to discretize the density function. The adaptive discretization may help to reduce this kind of error. However, it does

not take into account the density function and hence it is not well suited to fully perform this task.

We have developed a complementary discretization algorithm that takes into account the variations of the density function. This density-based discretization happens prior to the adaptive discretization described in the previous section. In short, the algorithm divides the tesseroid along the radial dimension at the depths at which the *maximum density variations* take place.

Consider an *original* tesseroid with density given by the function  $\rho(r')$ . Before the density-based discretization starts, we normalise the density function to the range  $[0, 1]$  as follows

$$\rho_n(r') = \frac{\rho(r') - \rho_{\min}}{\rho_{\max} - \rho_{\min}}, \quad (19)$$

in which  $\rho_{\min}$  and  $\rho_{\max}$  are the minimum and maximum density values inside the tesseroid boundaries. We emphasize that this normalised density function will not be modified throughout the algorithm. In case the density function is constant, both maximum and minimum densities will be equal and the density-based discretization algorithm will not be applied.

The algorithm is comprised of the following steps (Fig. 2):

*Step 1:* Define a linear function  $\rho_l(r')$  that assumes the same values as the normalised density  $\rho_n(r')$  at the boundaries of the tesseroid ( $r_1$  and  $r_2$ ):

$$\rho_l(r') = \frac{\rho_n(r_2) - \rho_n(r_1)}{r_2 - r_1}(r' - r_1) + \rho_n(r_1), \quad (20)$$

*Step 2:* Evaluate the normalized and linear density functions on a range of  $N$  radii between  $r_1$  and  $r_2$ . We have opted for  $N = 101$  but the specific value of  $N$  is not critical to the algorithm.

*Step 3:* Compute the absolute difference between the values of the linear and normalised density functions:

$$\Delta\rho(r') = |\rho_n(r') - \rho_l(r')|. \quad (21)$$

*Step 4:* If the following inequality holds, the tesseroid will not be divided:

$$\max\{\Delta\rho(r')\} \frac{L_r}{L_r^{\text{orig}}} \leq \delta, \quad (22)$$

in which  $L_r$  is the radial dimension of the tesseroid being considered for division,  $L_r^{\text{orig}}$  is the radial dimension of the original tesseroid, and  $\delta$  is a positive constant henceforth called the *delta ratio*.

*Step 5:* If inequality 22 is not satisfied, then the tesseroid is split in two parts at the radius  $r_{\max}$  at which the maximum absolute difference (Eq. 21) takes place.

*Step 6:* Repeat steps 1-6 for each smaller tesseroid produced in step 5.

Once all smaller tesseroids satisfy Eq. 22, each one is subjected to the adaptive discretization algorithm described earlier to calculate their gravitational effects.

On the first iteration, the ratio  $L_r/L_r^{\text{orig}} = 1$  because the tesseroid being divided is the original one. For future iterations, the ratio will be progressively smaller than one as the tesseroids get smaller. This is intended to limit the number of divisions to the ones that will significantly reduce the numerical error: dividing a large tesseroid with a small  $\max\{\Delta\rho(r')\}$  would improve the integration accuracy more than dividing a small tesseroid with a higher  $\max\{\Delta\rho(r')\}$ . We also do not divide tesseroids with  $L_r < 1$  mm

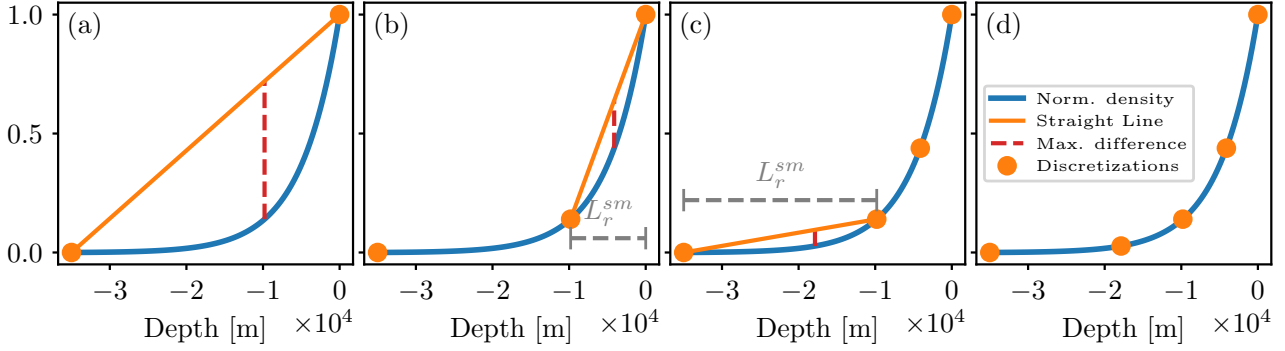


**Figure 2.** Example application of the density-based discretization algorithm to a non-linear density function. (a) the normalised density function  $\rho_n(r')$  (blue), current boundaries of the tesseroide (orange dots), and the linear density function  $\rho_l(r')$  (orange line). The dashed red line represents the maximum density difference  $\Delta\rho(r')$  at which the tesseroide would be divided (assuming that the inequality 22 is not satisfied). (b) second iteration of the algorithm with a new linear density function and maximum density difference. The tesseroide would be divided at the depth indicated by the dashed red line. (c) third iteration of the algorithm. (d) final output of the density-based discretization, assuming that all four new tesseroide satisfy inequality 22.

because any integration errors would be negligible due to the small mass of the tesseroide.

The higher  $\delta$  is, the fewer divisions will be made, and vice-versa. Thus, it controls how many times the tesseroide will be divided based on the density function and, indirectly, determines the accuracy and computation time of numerical integration. This raises the need to determine a maximum value of  $\delta$  that ensures an acceptable accuracy while minimising the computation time.

## 2.4 Software implementation

We have implemented the algorithms described in the previous sections in the Python programming language. The software is based on the pre-existing code for the homogeneous density tesseroide (Uieda et al. 2016), more specifically the implementation in the Python library *Fatiando a Terra* v0.5 (Uieda et al. 2013). The more time consuming parts of the algorithm are written in the Cython language to achieve higher performance. This new code is freely available under the BSD 3-clause open-source license. It can be downloaded from the online repository [github.com/pingalab/tesseroide-variable-density](https://github.com/pingalab/tesseroide-variable-density).

## 3 DETERMINATION OF THE DISTANCE-SIZE AND DELTA RATIOS

The distance-size ratio  $D$  of the adaptive discretization and the delta ratio  $\delta$  of the density-based discretization determine how many times each tesseroide will be divided and thus indirectly control the numerical error of the integration. Optimal values for  $D$  and  $\delta$  must be determined in order to ensure both acceptable numerical accuracy and computation efficiency for the algorithm.

Uieda et al. (2016) compared the numerical integration of homogeneous density tesseroide with the analytical solution of a spherical shell (Mikuška et al. 2006; Grombein et al. 2013) in order to obtain default values for the distance-size ratio  $D$ . We will follow this idea but for our needs the spherical shell must have the same density function of radius as our tesseroide model. Analytical solutions for a variable density spherical shell are not present in the literature and so they must be obtained first. We derive the expres-

**Table 1.** Description of the computation grids used to characterize the accuracy of the numerical integration. All grids consist of a set of  $10 \times 10$  points.

| Name      | Grid size                  | Grid region (degrees) | Grid height (km) |
|-----------|----------------------------|-----------------------|------------------|
| Pole      | $1^\circ \times 1^\circ$   | 0E/1E/89N/90N         | 2                |
| Equator   | $1^\circ \times 1^\circ$   | 0E/1E/0N/1N           | 2                |
| Satellite | $1^\circ \times 1^\circ$   | 0E/1E/89N/90N         | 260              |
| Big Grid  | $30^\circ \times 30^\circ$ | 0E/30E/60N/90N        | 2                |

sions for the gravitational fields of spherical shells with linear and exponential density functions of radius in Appendix A.

We perform comparisons between the analytical solutions for the spherical shell and the numerical integration results for linear and exponential density functions. From these results, we generalize default values for  $D$  and  $\delta$  that ensure a numerical error lower than 0.1% of the spherical shell values.

## 3.1 Linear Density

A spherical shell with a linear density function given by

$$\rho(r') = ar' + b, \quad (23)$$

has an analytical solution given by Eq. A.12.

The absolute density difference defined on equation 21 will always be zero for the linear density case. As a result, the inequality 22 will always be satisfied and no divisions will ever be performed. Therefore, the distance-size ratio  $D$  of the adaptive discretization algorithm is the only mechanism that controls the accuracy of the numerical integration. For this reason, we will only determine the minimum value of  $D$  needed in order to guarantee an acceptable accuracy while ignoring the value of  $\delta$ .

In order to compare the numerical results with the analytical solution we must build a spherical shell made of tesseroide. The outer radius of the shell is equal to the mean Earth radius and we repeat the calculations for shell thicknesses of 1km and 35km. We discretize the shell into a single layer of  $30^\circ \times 30^\circ$  tesseroide and compute their gravitational effects on  $10 \times 10$  point grids with different resolutions, heights, and locations on the sphere. These grids

are defined in Table 1. The density of the shell and tesseroid model varies linearly with  $r$  (Eq. 23) with angular coefficient

$$a = -\frac{3300\text{kg/m}^3 - 2670\text{kg/m}^3}{R - R_1}, \quad (24)$$

and linear coefficient

$$c = \frac{3300\text{kg/m}^3 - 2670\text{kg/m}^3}{R - R_1} R + 2670\text{kg/m}^3, \quad (25)$$

in which  $R = 6378.137$  km is the mean Earth radius and  $R_1$  is the inner radius of the shell (determined by the thickness).

We compute the gravitational potential ( $V$ ), the vertical component of the gradient ( $g_z$ ), and the diagonal components of the Marussi tensor ( $g_{xx}$ ,  $g_{yy}$ ,  $g_{zz}$ ) for each grid in Table 1. Other components are equal to zero outside of the shell and are thus omitted from the analysis. The computations are repeated for values of  $D$  ranging from 0.5 to 10 with a step of 0.5. We will then calculate the maximum absolute difference between these results and the analytical solutions derived in Appendix A. The differences are shown in Fig. 3 as relative to the spherical shell values. We omit the differences for  $g_{xx}$  and  $g_{yy}$  because they are equivalent to the ones obtained for  $g_{zz}$ . Finally, we set the optimal value of  $D$  as the minimum value at which the corresponding error of the numerical approximation is lower than 0.1%.

We observe from Fig. 3 that the relative errors for the potential and the  $g_z$  component fall below the 0.1% threshold at  $D = 1$  and  $D = 2$ , respectively, for both shell thicknesses. On the other hand,  $g_{zz}$  displays a noticeable difference between the thin and the thick shell: the first one needs a value of  $D$  equal to 8 while the later only a  $D$  of 3.

### 3.2 Exponential Density

For an exponential density function, the density-based discretization will be applied before the adaptive discretization algorithm. This means that optimal values for both the distance-size ratio  $D$  and the delta ratio  $\delta$  must be determined. We perform an error analysis similar to what was done for the linear density case. However, we only consider the “Big Grid” from Table 1 for the sake of brevity.

The spherical shell and tesseroid model will have an exponential density function given by

$$\rho(r') = Ae^{-(r'-R)/b} + C, \quad (26)$$

where

$$A = (3300\text{kg/m}^3 - 2670\text{kg/m}^3) \left( e^{(R-R_1)/b} - 1 \right)^{-1}, \quad (27)$$

$$C = 2670\text{kg/m}^3 - A, \quad (28)$$

$R$  is the mean Earth radius,  $R_1$  is the inner radius of the shell (determined by the thickness), and  $b$  is a constant that determines the variability of the function: a low value of  $b$  increases the maximum slope of the density function.

#### 3.2.1 $D$ - $\delta$ space exploration

We aim to find a combination of the  $D$  and  $\delta$  that produces a numerical error lower than the 0.1% threshold while minimizing computation time. We use a grid search method and compute the numerical error for every  $(D, \delta)$  pair belonging to a grid on the  $D$ - $\delta$  space (Fig. 4). Because this is a time consuming computation, we limit the analysis to a shell of 35 km thickness and  $b = 1$  km (Eq. 26), which yields a sharp density variation within the shell. For optimum algorithm performance, we search for the smallest possible value of  $D$  and the highest possible value of  $\delta$ .

We compute the relative difference between the numerical and analytical results for the gravitational potential ( $V$ ), the vertical component of its gradient ( $g_z$ ), and the  $g_{zz}$  component of the Marussi tensor. The results are shown in Fig. 4, in which points inside the dotted lines are the ones that present a numerical error lower than the 0.1% threshold. Also shown in Fig. 4 are the  $D$  values determined for the linear density function in the previous section ( $D_{\text{linear}}$ ). The values of  $D_{\text{linear}}$  are within the 0.1% threshold and are the optimum values of  $D$  for  $V$  and  $g_z$ . The results for  $g_{zz}$  are in agreement with those obtained for the linear density function in the case of a thick shell (Fig. 3). Thus, we also choose the conservative value of  $D = 8$  as the optimum value for  $g_{zz}$ . These results indicate that the values of  $D_{\text{linear}}$  can be safely extrapolated to the exponential case.

#### 3.2.2 Delta ratio determination

Having chosen values of  $D$  equal to linear density case, we are free to explore the integration error as a function of  $\delta$  in more detail and how it varies for different values of  $b$  (Eq. 26). We perform the error calculations for the “Big Grid” configuration (Table 1) for two spherical shell models with 1km and 35km thickness. The calculations are repeated for different values of  $b$  to examine the error variation with the sharpness of the density function. Because larger  $\delta$  values result in fewer tesseroid divisions, our intention is to find the highest value of  $\delta$  whose numerical error is below the 0.1% threshold.

Fig. 5 shows the density functions and the resulting relative differences ( $V$ ,  $g_z$ , and  $g_{zz}$ ) for different values of  $b$  and thickness of the shell and tesseroid model. The relative difference for  $V$  and  $g_z$  falls below the 0.1% threshold for  $\delta = 0.2$  in both the thick and thin shell cases. On the other hand, optimal values of  $\delta$  for  $g_{zz}$  are  $\delta = 0.2$  for the thin shell and  $\delta = 0.01$  for the thick shell. Once again, we opt for the conservative value of  $\delta = 0.01$  and sacrifice performance for the sake of accuracy.

## 4 APPLICATION TO THE NEUQUÉN BASIN

We applied the new algorithms and optimal values of  $D$  and  $\delta$  determined previously to calculate the gravitational effects of the Neuquén Basin: a sedimentary basin located to the east of the Andes, between 32°S and 40°S latitude (Fig. 6a). The basin includes continental and marine siliciclastics, carbonates, and evaporites accumulated over the Jurassic and the Cretaceous constituting a stratigraphic record up to 5000m of depth (Howell et al. 2005).

The thickness of the sediment pack was digitized from Heine (2007) on a regular grid with a resolution of 0.05° on both longitude and latitude directions (Fig. 6b). We created a tesseroid model of the sediment pack by placing a 0.05° × 0.05° tesseroid on each



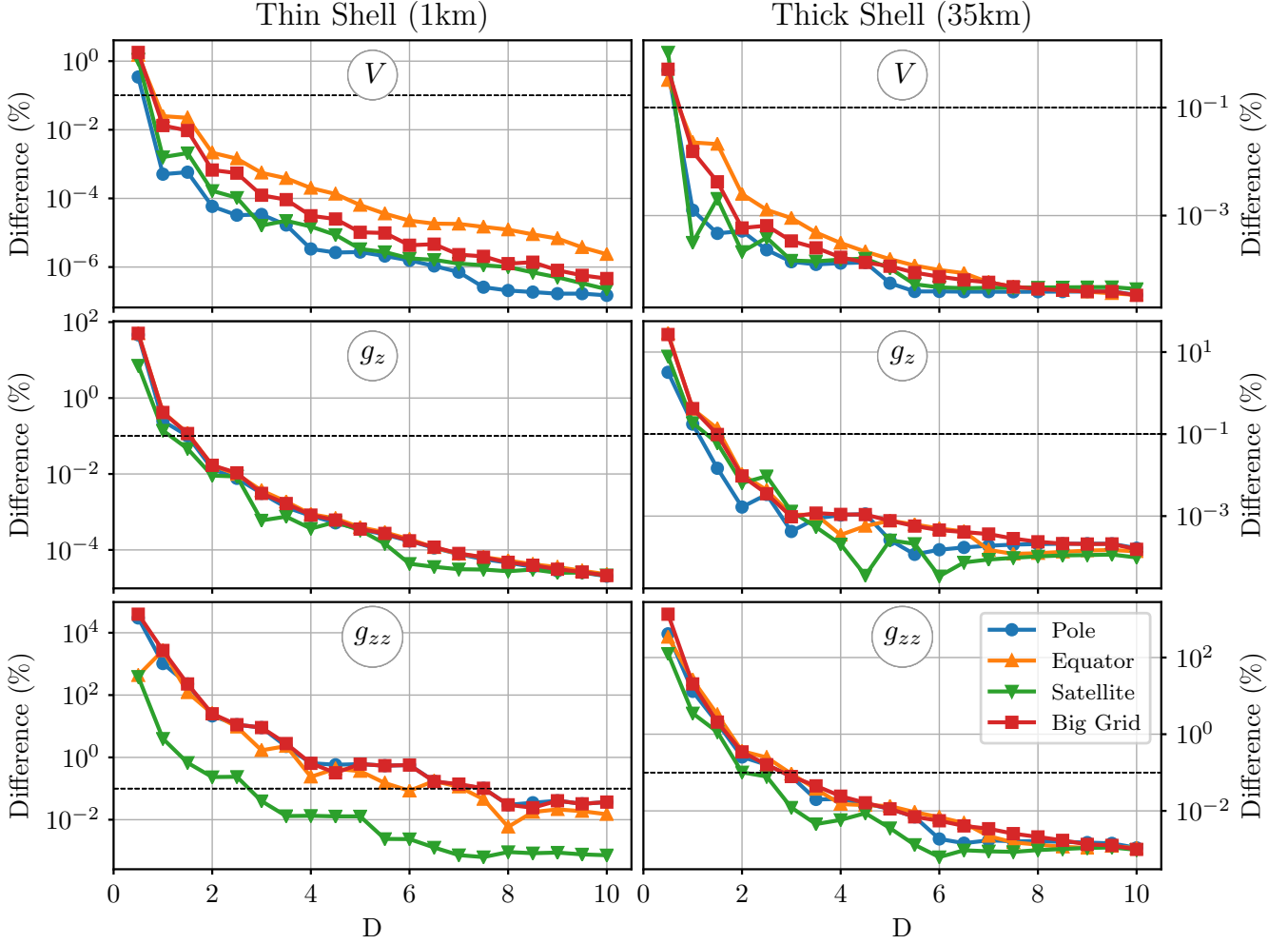


**Figure 3.** Differences between the gravitational fields generated by the tesseroïd model and the analytical solution for a thin (left) and a thick (right) spherical shell. Both models have a linear density function of radius (Eq. 23). The computations were performed on the four combinations described in Table 1. Due to the linearity of the density function, the density-based discretization algorithm is not applied. Differences are reported as a percentage of the shell values. The horizontal dashed black line represents a target difference of 0.1%.

node of the grid. The top of each tesseroïd was fixed at 0 m depth and the bottom at corresponding thickness of the basin.

We must also define a density function for the tesseroïd model. Sigismondi (2012) measured a minimum and maximum density contrast for the Neuquén basin of  $-412\text{kg/m}^3$  and  $-275\text{kg/m}^3$ , respectively. We have chosen an exponential density variation (Eq. 26) that assumes the minimum value on the top surface and the maximum at 5858m depth (the thickest part of the basin), with a value of  $b$  equal to 2km. This density function can be seen on Fig. 6c.

Finally, we computed the gravitational potential  $V$ , gradient components  $g_x$ ,  $g_y$  and  $g_z$ , and the Marussi tensor components  $g_{xx}$ ,  $g_{xy}$ ,  $g_{xz}$ ,  $g_{yy}$ , and  $g_{zz}$  on a computation grid of  $159 \times 163$  nodes ( $0.05^\circ$  spacing on both longitude and latitude) at a 50km height over the reference ellipsoid. The resulting fields can be seen in Fig. 6d-l. We have excluded the other components of the Marussi tensor from the Fig. 6, although they can be found in the online repository.

## 5 CONCLUSIONS

We have developed a new methodology to compute the gravitational fields generated by a tesseroïd with a density given by a continuous function of depth. It numerically solves the integrals that define the gravitational potential, its gradient, and the Marussi tensor components through the Gauss-Legendre Quadrature (GLQ). The accuracy of the numerical integration is automatically controlled by an adaptive discretization algorithm and a new density-based discretization algorithm. The former divides the tesseroïd in half if the ratio of the distance to the computation point and the size of the tesseroïd is lower than a predefined distance-size ratio  $D$ . This algorithm minimises the integration error when the computation point is close to the tesseroïd. Nevertheless, the adaptive discretization alone is not sufficient to guarantee the accuracy of the method in case of tesseroïds with variable density.

To overcome this challenge, we have developed a density-based discretization algorithm that divides the tesseroïd on the points at which the maximum variations of the density function take place. The density-based discretization is performed before adaptive discretization as a type of pre-processing step. The number of

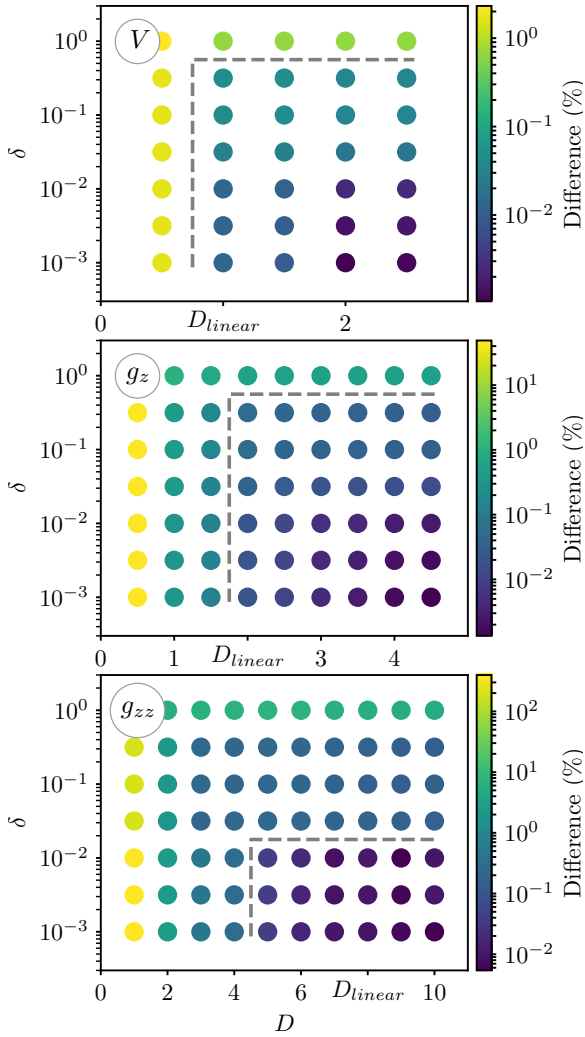


**Figure 4.** Numerical error exploration in the  $D$ - $\delta$  space. The percentage difference values were obtained from the comparison between the analytical solution and the numerical approximation of the gravitational fields ( $V$ ,  $g_z$  and  $g_{zz}$ ) generated by a spherical shell with an exponential density function (Eq. 26). These comparisons were carried out on the “Big Grid” (Table 1), with a spherical shell of 35km of thickness, and density function with  $b$  of 1km. The points inside the dashed line are the ones that present an error lower than 0.1%.

divisions performed, and thus the accuracy of the computation, is controlled by the delta ratio  $\delta$ . This new algorithm is intended to minimise the error due to the inability of the GLQ to produce precise approximations of density functions with sharp variations.

Because there is no direct relation between the values assigned to  $D$  and  $\delta$  and the error of the computation, we empirically determined the optimum values for these parameters. These values minimize the computational load while maintaining the numerical error below 0.1% of an analytical solution. The density functions used to establish the optimum values were a linear and an exponential function. The linear function represents the smoothest variation of density and does not require density-based discretization at all. We analysed the error for exponential functions ranging from smooth to sharp variations in depth to test the accuracy of the density-based discretization. Through this analysis, we have obtained optimal values for the distance-size ratio of 1, 2 and 8 for the potential, its gradient, and the Marussi tensor components, respectively. These

values are in agreement with previous results for a homogeneous density tesseroid. The optimum  $\delta$  values are 0.2 for the potential and its gradient components, while a  $\delta = 0.01$  must be used for the Marussi tensor components in order to ensure a 0.1% precision. A wide range of exponential functions were used to infer these results and they are conservative estimates, chosen to prioritize accuracy over speed of computations. Therefore, they can be safely generalized to other common depth-density relations, like quadratic functions, without loss of accuracy.

## 6 ACKNOWLEDGMENTS

We are indebted to the developers and maintainers of the open-source software without which this work would not have been possible.

## REFERENCES

- Asgharzadeh, M., Von Frese, R., Kim, H., Leftwich, T., & Kim, J., 2007. Spherical prism gravity effects by Gauss-Legendre quadrature integration, *Geophysical Journal International*, **169**(1), 1–11.
- Cordell, L., 1973. Gravity analysis using an exponential density-depth function – San Jacinto Graben, California, *Geophysics*, **38**(4), 684–690.
- Cowie, P. A. & Karner, G. D., 1990. Gravity effect of sediment compaction: examples from the North Sea and the Rhine Graben, *Earth and Planetary Science Letters*, **99**(1), 141–153.
- Grombein, T., Seitz, K., & Heck, B., 2013. Optimized formulas for the gravitational field of a tesseroid, *Journal of Geodesy*, **87**(7), 645–660.
- Heck, B. & Seitz, K., 2007. A comparison of the tesseroid, prism and point-mass approaches for mass reductions in gravity field modelling, *Journal of Geodesy*, **81**(2), 121–136.
- Heine, C., 2007. *Formation and evolution of intracontinental basins*, Ph.D. thesis, School of Geosciences, The University of Sydney, Australia.
- Hildebrand, F. B., 1987. *Introduction to numerical analysis*, Courier Corporation.
- Howell, J. A., Schwarz, E., Spalletti, L. A., & Veiga, G. D., 2005. The Neuquén basin: an overview, *Geological Society, London, Special Publications*, **252**(1), 1–14.
- Ku, C. C., 1977. A direct computation of gravity and magnetic anomalies caused by 2- and 3-dimensional bodies of arbitrary shape and arbitrary magnetic polarization by equivalent-point method and a simplified cubic spline, *Geophysics*, **42**(3), 610–622.
- Li, Z., Hao, T., Xu, Y., & Xu, Y., 2011. An efficient and adaptive approach for modeling gravity effects in spherical coordinates, *Journal of Applied Geophysics*, **73**(3), 221–231.
- Maxant, J., 1980. Variation of density with rock type, depth, and formation in the Western Canada Basin from density logs, *Geophysics*, **45**(6), 1061–1076.
- Meurer, A., Smith, C. P., Paprocki, M., Čertík, O., Kirpichev, S. B., Rocklin, M., Kumar, A., Ivanov, S., Moore, J. K., Singh, S., Rathnayake, T., Vig, S., Granger, B. E., Muller, R. P., Bonazzi, F., Gupta, H., Vats, S., Johansson, F., Pedregosa, F., Curry, M. J., Terrel, A. R., Roučka, v., Saboo, A., Fernando, I., Kulal, S., Cimrman, R., & Scopatz, A., 2017. SymPy: symbolic computing in Python, *PeerJ Computer Science*, **3**, e103.
- Mikuška, J., Pašteka, R., & Marušák, I., 2006. Estimation of distant relief effect in gravimetry, *Geophysics*, **71**(6), J59–J69.
- Rao, C. V., Chakravarthi, V., & Raju, M., 1993. Parabolic density function in sedimentary basin modelling, *pure and applied geophysics*, **140**(3), 493–501.
- Rao, C. V., Chakravarthi, V., & Raju, M., 1994. Forward modeling: Gravity anomalies of two-dimensional bodies of arbitrary shape with hyperbolic and parabolic density functions, *Computers & Geosciences*, **20**(5), 873–880.

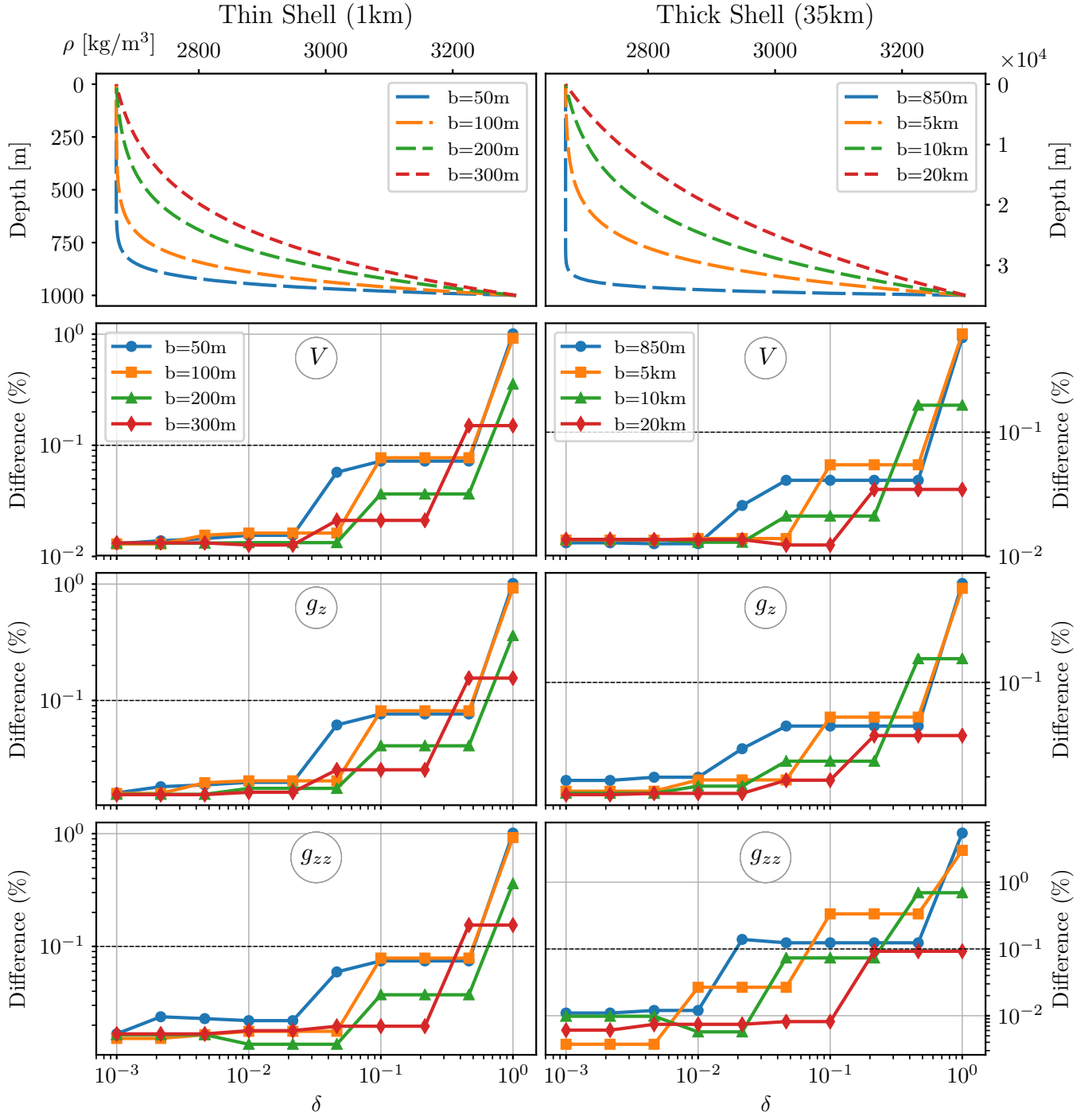


**Figure 5.** Numerical error for different exponential density functions and values of the delta ratio. The top panels show the exponential density functions for different values of  $b$  (Eq. 26). The error computations were performed on the “Big Grid” configuration described in Table 1, with fixed values of the distance-size ratio  $D$  obtained for the linear density case ( $D = 1, 2, 8$  for the potential, gradient components, and tensor components, respectively). The difference is reported as a percentage of the shell values.

Rao, D. B., 1986. Modelling of sedimentary basins from gravity anomalies with variable density contrast, *Geophysical Journal International*, **84**(1), 207–212.

Sigismundi, M. E., 2012. *Estudio de la deformación litosférica de la cuenca Neuquina: estructura termal, datos de gravedad y sísmica de reflexión*, Ph.D. thesis, Facultad de Ciencias Exactas y Naturales, Universidad de Buenos Aires.

Uieda, L., 2015. A tesseroid (spherical prism) in a geocentric coordinate

system with a local-North-oriented coordinate system, figshare, available from: <http://dx.doi.org/10.6084/m9.figshare.1495525>, Accessed 17 July 2017.

Uieda, L., Oliveira Jr, V. C., & Barbosa, V. C. F., 2013. Modeling the Earth with Fatiando a Terra, in *Proceedings of the 12th Python in Science Conference*, pp. 96–103.

Uieda, L., Barbosa, V. C., & Braitenberg, C., 2016. Tesseroids: Forward-modeling gravitational fields in spherical coordinates, *Geophysics*, **81**(5),



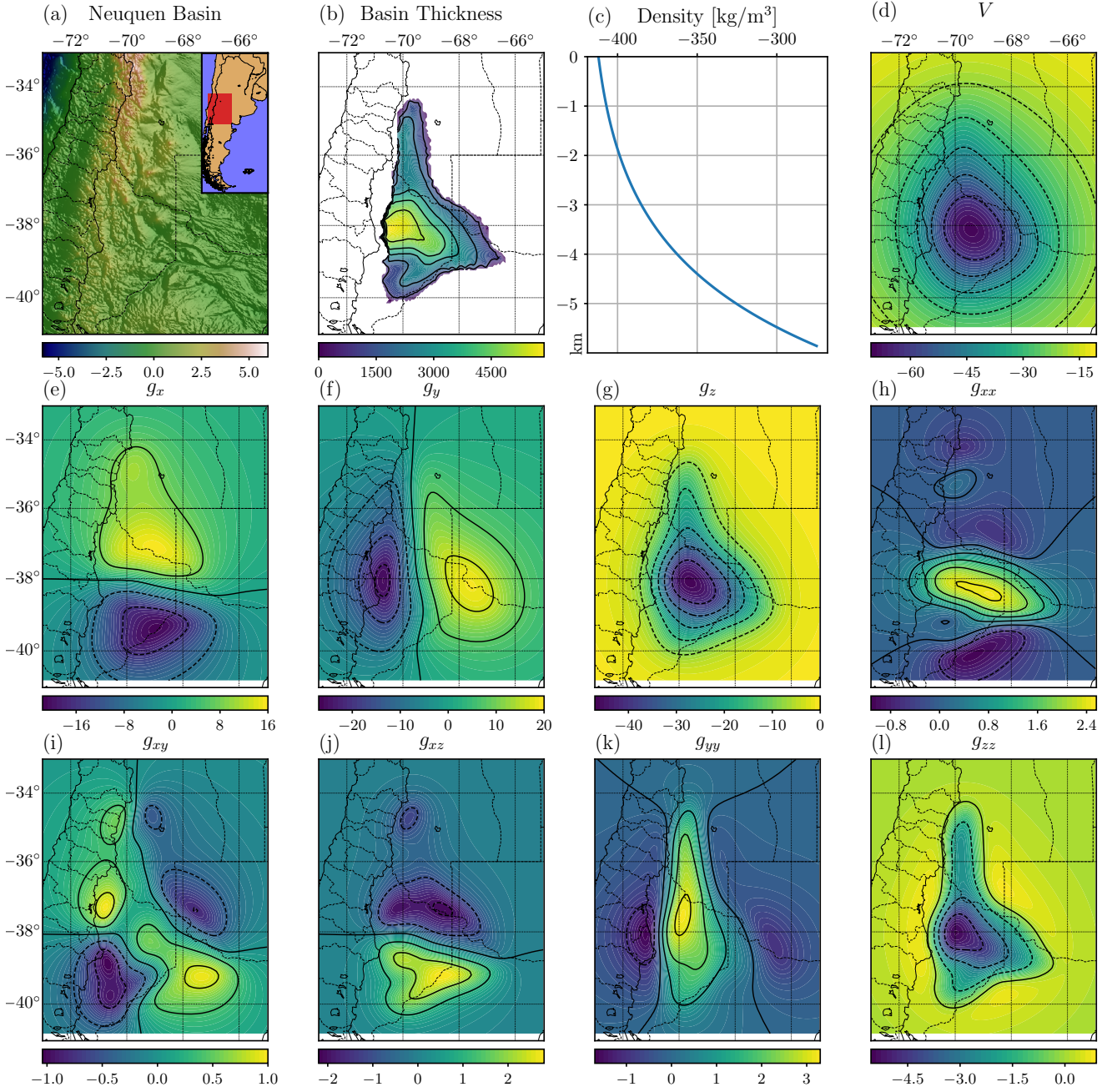


**Figure 6.** Gravitational effects of the Neuquén sedimentary basin modelled using tesseroids with an exponential density function of depth. (a) Topography of the Neuquén Basin (in km) and its location in South America, (b) thickness of the sedimentary basin (in meters; Heine 2007), (c) the exponential density function used to model the basin (depth in km and density in  $\text{kg/m}^3$ ), (d)–(l) computed gravitational fields: potential  $V$  (in  $\text{J/kg}$ ), gradient components  $g_x$ ,  $g_y$  and  $g_z$  (in  $\text{mGal}$ ), and Marussi tensor components (in Eötvös), calculated at 50km of height over the ellipsoid.

F41–F48.

Welford, J. K., Shannon, P. M., O'Reilly, B. M., & Hall, J., 2010. Lithospheric density variations and Moho structure of the Irish Atlantic continental margin from constrained 3-D gravity inversion, *Geophysical Journal International*, **183**(1), 79–95.

Wild-Pfeiffer, F., 2008. A comparison of different mass elements for use in gravity gradiometry, *Journal of Geodesy*, **82**(10), 637–653.

Zhang, J., Zhong, B., Zhou, X., & Dai, Y., 2001. Gravity anomalies of 2D bodies with variable density contrast, *Geophysics*, **66**(3), 809–813.

## APPENDIX A: ANALYTICAL SOLUTIONS FOR SPHERICAL SHELL

Consider a spherical shell with inner radius  $R_1$  and outer radius  $R_2$ , whose density is a function  $\rho(r')$  of the radial coordinate (Fig. A1). The gravitational potential generated by the shell on an arbitrary external point  $Q$  can be written as follows:

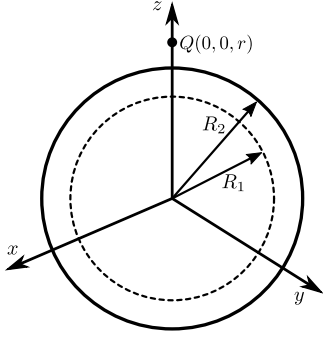


**Figure A1.** Spherical shell with inner and outer radii  $R_1$  and  $R_2$ , respectively. The computation point  $Q$  is located on the  $z$  axis at a distance  $r$  from the origin of the coordinates system. For our purposes we will assume that  $Q$  is outside of the shell, i.e.  $r > R_2$ .

$$V_{\text{sh}}(\phi, \lambda, r) = G \int_0^{2\pi} \int_{-\pi/2}^{\pi/2} \int_{R_1}^{R_2} \frac{\rho(r') r'^2 \cos \phi'}{\ell} dr' d\phi' d\lambda', \quad (\text{A.1})$$

where  $\ell$  is defined in equation 9.

For  $Q$  located along the  $z$  axis (i.e.,  $\phi = 90^\circ$ ) at a distance  $r$  from the origin, equation 9 simplifies to:

$$\ell = \sqrt{r'^2 + r^2 - 2rr' \sin \phi'}. \quad (\text{A.2})$$

Because of the rotational symmetry along the  $z$  axis, the integration in  $\lambda'$  is straightforward:

$$V_{\text{sh}}(r) = 2\pi G \int_{-\pi/2}^{\pi/2} \int_{R_1}^{R_2} \frac{\rho(r') r'^2 \cos \phi'}{\sqrt{r'^2 + r^2 - 2rr' \sin \phi'}} dr' d\phi', \quad (\text{A.3})$$

while the integration in  $\phi'$  can be performed independently of the density function. Making use of SymPy (Meurer et al. 2017), a Python library for symbolic mathematics, we obtained the following expression for the potential:

$$V_{\text{sh}}(r) = 2\pi G \int_{R_1}^{R_2} \left[ \sqrt{r^2 + r'^2 + 2rr'} - \sqrt{r^2 + r'^2 - 2rr'} \right] \frac{r' \rho(r')}{r} dr'. \quad (\text{A.4})$$

Because the computation point  $Q$  is outside of the shell,  $r > r'$  and the square roots in equation A.4 simplify to

$$\sqrt{r^2 + r'^2 + 2rr'} = |r + r'| = r + r', \quad (\text{A.5})$$

$$\sqrt{r^2 + r'^2 - 2rr'} = |r - r'| = r - r', \quad (\text{A.6})$$

which leads to the following expression for the potential:

$$V_{\text{sh}}(r) = \frac{4\pi G}{r} \int_{R_1}^{R_2} r'^2 \rho(r') dr'. \quad (\text{A.7})$$

The gradient and the Marussi tensor of potentials that depends

solely on  $r$  have only a few non zero components: the vertical component of the gradient ( $g_z$ ) and the diagonal components of the tensor ( $g_{xx}$ ,  $g_{yy}$ ,  $g_{zz}$ ). Following Grombein et al. (2013):

$$g_z(r) = \frac{V_{\text{sh}}(r)}{r}, \quad (\text{A.8})$$

$$g_{xx}(r) = g_{yy}(r) = -\frac{V_{\text{sh}}(r)}{r^2} \quad (\text{A.9})$$

$$g_{zz}(r) = \frac{2V_{\text{sh}}(r)}{r^2}. \quad (\text{A.10})$$

From Eq. A.7 we can obtain expressions for gravitational potential for different density functions. For a linear density function

$$\rho(r') = ar' + b, \quad (\text{A.11})$$

the gravitational potential at any external point is

$$V_{\text{sh}}^{\text{lin}}(r) = \pi G \left[ a \frac{R_2^4 - R_1^4}{r} + b \frac{4}{3} \frac{R_2^3 - R_1^3}{r} \right]. \quad (\text{A.12})$$

The first term on this equation reproduces the potential generated by a spherical shell with variable density  $\rho(r') = ar'$ , while the second term constitutes the potential generated by a spherical shell with homogeneous density  $\rho = b$  (Mikuška et al. 2006; Grombein et al. 2013).

An exponential density function that assumes the values of  $\rho_{\text{out}}$  and  $\rho_{\text{in}}$  on the shell's outer and inner surfaces, respectively, can be defined as follows:

$$\rho(r') = Ae^{-(r'-R)/b} + C, \quad (\text{A.13})$$

where

$$A = (\rho_{\text{in}} - \rho_{\text{out}}) \left( e^{(R_2 - R_1)/b} - 1 \right)^{-1}, \quad (\text{A.14})$$

$$C = \rho_{\text{out}} - A, \quad (\text{A.15})$$

$R$  is the mean Earth radius, and  $b$  is a constant that determines the variability of the function: a low value of  $b$  increases the maximum slope of the density function.

The analytical solution of the gravitational potential generated by a spherical shell with a density function is

$$V_{\text{sh}}^{\text{exp}}(r) = \frac{4\pi G}{r} Ab \left[ (R_1^2 + 2R_1b + 2b^2) e^{-\frac{R_1 - R}{b}} - (R_2^2 + 2R_2b + 2b^2) e^{-\frac{R_2 - R}{b}} \right] + \frac{4\pi G}{3r} C (R_2^3 - R_1^3). \quad (\text{A.16})$$